applied sciences

MDPI

Article

Design and Additive Manufacturing of TPMS Heat Exchangers

Jian Liu *, David Cheng, Khin Oo, Ty-Liyiah McCrimmon and Shuang Bai

PolarOnyx, Inc., 144 Old Lystra Road, Unit 2, Chapel Hill, NC 27517, USA
* Correspondence: jianliu@polaronyx.com

Abstract: Triply periodic minimal surface (TPMS) heat exchangers (HXs) have been investigated in this paper along with additive manufacturing (AM). Heat transfer coefficients, pressure drops, and thermal capacity were systematically evaluated as functions of wall thickness, lattice cell density, and materials. It turns out that when thermal conductivity is above 100 W/m·K, gyroid HXs are less sensitive to variations in thickness and thermal conductivity. Additive manufacturing of 20 kW aluminum heat exchangers was successful and testing results are comparable with theoretical prediction. To the best of our knowledge, this is the first demonstration of a working prototype of TPMS HXs.

Keywords: additive manufacturing; laser 3D printing; triply periodic minimal surface (TPMS); heat exchanger; gyroid; aluminum; thermal management

Citation: Liu, J.; Cheng, D.; Oo, K.; McCrimmon, T.-L.; Bai, S. Design and Additive Manufacturing of TPMS Heat Exchangers. *Appl. Sci.* **2024**, *14*, 3970. https://doi.org/10.3390/app14103970

Academic Editor: Sasan Dadbakhsh

Received: 11 March 2024
Revised: 15 April 2024
Accepted: 5 May 2024
Published: 7 May 2024

1. Introduction

Heat exchangers (HXs) are present in all major industrial fields, being an essential component of most engineering systems. The design of an HX is a balance between maximizing the surface area in order to transfer heat and minimizing the pressure drop of the HX. In the aviation and automotive industries, compact HXs were widely used thanks to their relatively small volumes and consequently low weights and high thermal efficiency [1]. It is very important to reduce the weight of HXs, by acting on the size/weight, while performance in terms of thermal efficiency must reach high levels [2]. In aeronautical and aerospace applications, the most commonly used HXs are the finned plate type due to their compactness, high efficiency, and ease of system integration. Most of the finned plates in compact HXs are parallel to each other. It is difficult to fabricate other geometries of the fins due to conventional manufacturing capabilities [3].

Modern additive manufacturing (AM) techniques provide new ways to manufacture HXs with complex geometries. Laser Powder Bed Fusion (L-PBF), previously called Selective Laser Melting (SLM), is a typical AM process that uses a laser beam as a heat source to fuse metal powders. The starting point of the process is the creation of a 3D CAD model, which is then sliced numerically into several finished layers by the software. For each sliced layer, a hatch pattern is defined and computed as a laser path. The path data is exported to a laser scanner. The laser beam is manipulated by the laser scanner to the layer to fuse the CAD model onto the layer of powder. The process is repeated layer by layer, and the melted powder particles solidify to form a component [4,5]. L-PBF is the most widely used metal AM technology in the world and is a promising technology for the printing of HXs with complex geometries. The L-PBF process also has challenges. It is difficult to create a high-quality, defect-free thin wall or thin features in general with a thickness of less than 200~300 μm. In addition, conventional manufacturing methods such as stamping have the capability to fabricate plate fins with typical thicknesses ranging from 46 to 200 μm [6,7].

The use of triply periodic minimal surfaces (TPMSs) has been proven to be a possible method to enhance the heat transfer and, consequently, the efficiency of a TPMS HX [8].

Figure 1 shows some examples of triply periodic minimal surfaces (TPMSs), such as gyroid, diamond, Schwarz, SplitP, etc. Due to their unique capability in providing high surface area-to-volume ratios and operating at high turbulent modes and high structure stiffnesses, these structures have been explored recently in relation to heat exchangers (HXs) and have achieved unprecedented performances, by taking advantages of additive manufacturing (AM) technology [9,10]. The TPMS-walled HXs, manufactured via AM, have great potential for industrial development. The relationships between heat transfer, pressure drop, and type of structure still need to be properly evaluated [11,12]. These TPMS-based core structures are not easy to design using existing CAD systems, especially in the case of HXs with complex 3D geometries [13]. In this paper, the commercial software nTop 4.23.2 (www.ntop.com) was used to model the TPMS HXs.

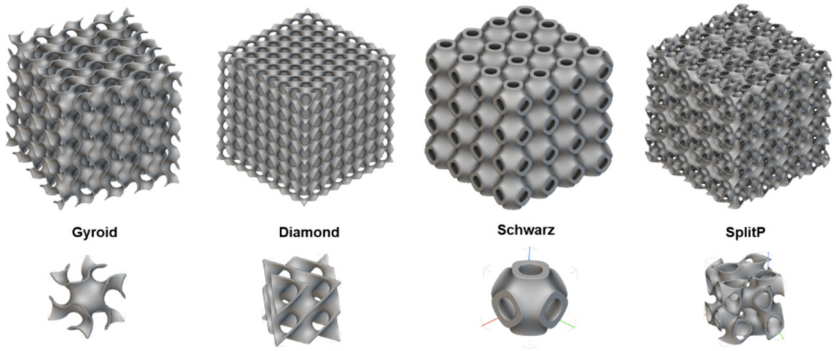

Figure 1. Various types of triply periodic minimal surface (TPMS) lattices.

Recently, studies about TPMS HX have used polymer composites that have some limitations: (a) low thermal conductivity, (b) failure at high operating pressure, or (c) high porosity in 3D printing. Tisha Dixit reported a microarchitected gyroid lattice liquid–liquid compact heat exchanger realized via stereolithography additive manufacturing as a single ready-to-use unit. The experimental results showed a 55% increase in exchanger effectiveness for the additively manufactured gyroid lattice heat exchanger in comparison to a common heat exchanger [14]. The Reynolds number in the 3D printed compact heat exchanger was relatively small. The turbulence in the compact HX should have been much higher. The material used in the printing had relatively low thermal conductivity. Mahmoud, D. et al. explored metal TPMS heat exchangers, which were used to transfer heat from air to liquid, and investigated the gyroid's geometric features including the network type, thickness, unit cell size, and aspect ratio. Mahmoud, D. et al. found that the LPBF-fabricated gyroid heat exchangers outperformed the conventional design [15].

TPMS HXs have a variety of applications where size, efficiency, weight and cost play important roles. These areas include space aircraft, defense, high-power electronics, nuclear energy, and waste energy recovery. For example, in space aircraft, TPMSs will resolve future challenges related to increased electrically powered subsystems and ultra-high bypass geared turbofan engines, as well as the possible advent of electrified or nuclear propulsion [16,17]. In high-power electronics, high-efficient cooling and flexible thermal management solutions meet critical demands with the continuous miniaturization and rapid increase in heat flux of electronic devices [18,19]. In waste energy recovery, there is a strong need to develop low-cost advanced heat exchangers that increase heat transfer coefficients and can withstand corrosive environments in heat recovery systems [20].

In this paper, a systematic investigation is undertaken, from design to manufacturing, on metal TPMS HXs, in consideration of material thermal conductivity, TPMS lattice types, lattice unit length, and wall thickness. Section 2 details the design and modeling of TPMS HXs. Section 3 describes TPMS HX fabrication with AM and its testing results. Section 4 discusses our conclusions.

2. Design and Modeling of TPMS HXs

2.1. Design Procedures of TPMS HXs

As shown in Table 1, the SplitP lattice has the highest surface area-to-volume ratio and Schwarz has the lowest surface-to-volume ratio at the same lattice unit length. The surface-to-volume ratio of different lattices increases linearly when the lattice unit length decreases.

Table 1. Parameters of the different types of TPMS lattice.

Lattice Type	Lattice Unit Length mm	Surface Area-to-Volume Ratio mm^{-1}
Gyroid	10 × 10 × 10	0.62
Diamond	10 × 10 × 10	0.78
Schwarz	10 × 10 × 10	0.48
SplitP	10 × 10 × 10	1.02

A conjugate heat transfer (CHT) model HX-40 in ANSYS Fluent was built in order to compare the performances of heat exchangers with different types of TPMS lattice. The steady state 3D flow field, including pressure, velocity and temperature, was calculated. The viscous model used in the analysis was an SST k-ω model. The energy equations were included in the simulation in order to calculate the heat transfer in the heat exchanger. The inlet boundary condition was a mass flow inlet, and the outlet boundary condition was a pressure outlet. The pressure of the outlet was 0 Pa. Two interfaces between the solid wall and fluid were created in order to transfer heat between the solid and the fluid. As shown in Figure 2, the core of the heat exchanger in the CHT model was cube shaped, with an edge length of 40 mm. The temperature field and velocity field were the simulation results that shown in Figure 3.

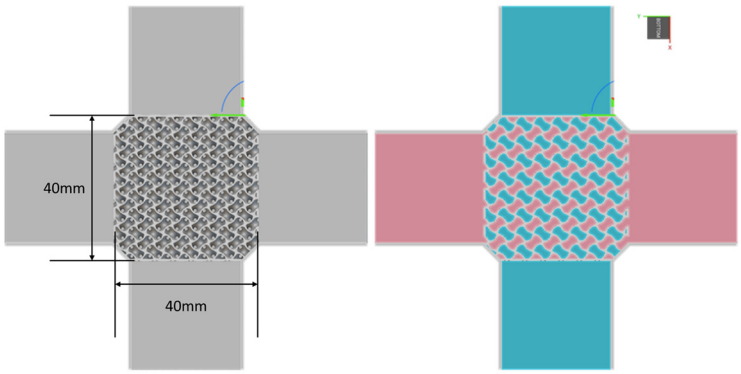

Figure 2. The CHT model HX-40, used to simulate different types of lattices. Grey color indicates the solid structure. Pink color indicates high temperature water. Light blue indicates the cold water.

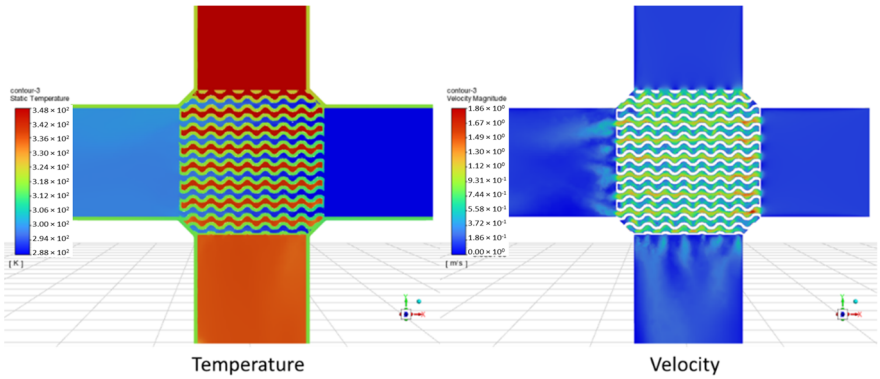

Figure 3. The simulation results for model HX-40.

The hot inlet temperature of the water was 348 K and the cold inlet temperature was 288 K. The flow rate range was 0.05~2 kg/s.

In Figure 4, for the HX-40 model, three different types of lattices were infilled in the HX core. As the volume of the core was the same, the unit lengths of different lattices were changed in order to keep the surface areas in the HX-40 the same as each other.

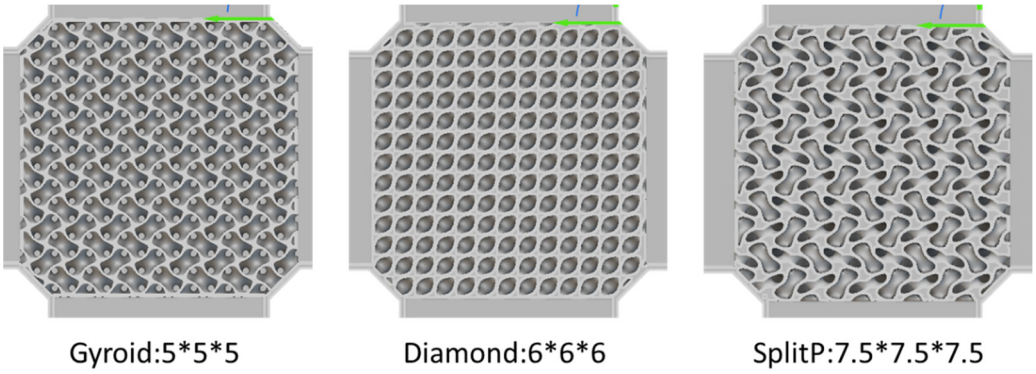

Figure 4. HX-40 core infilled with different lattices.

The input parameters of HX-40 and the simulation results such as the heat transfer power, HTC and HTC×A are shown in Table 2.

Table 2. Simulation results for different lattices.

No.	Lattice Type	Lattice Unit Length mm	Surface Area m^2	Flow Rate kg/s	Heat Transfer Power KW	Pressure Drop Pa	HTC×A W/K	HTC W/(K*m^2)
1	Gyroid	5 × 5 × 5	0.037	0.1	7.15	1768	167	4523
2	Gyroid	5 × 5 × 5	0.037	0.2	9.96	5750	208	5629
3	Gyroid	5 × 5 × 5	0.037	0.5	17.35	30,253	338	9122
4	Gyroid	5 × 5 × 5	0.037	2	44.58	435,583	820	22,169
1	Diamond	6 × 6 × 6	0.039	0.1	7.5	1707	177	4545
2	Diamond	6 × 6 × 6	0.039	0.2	9.8	5860	204	5231
3	Diamond	6 × 6 × 6	0.039	0.4	14.3	21,520	278	7125
4	Diamond	6 × 6 × 6	0.039	2.0	46.0	499,229	844	21,648
1	SplitP	7.5 × 7.5 × 7.5	0.041	0.1	7.2	2365	181	4406
2	SplitP	7.5 × 7.5 × 7.5	0.041	0.2	10.5	7922	233	5693
3	SplitP	7.5 × 7.5 × 7.5	0.041	0.4	15.2	27,843	313	7625
4	SplitP	7.5 × 7.5 × 7.5	0.041	2.0	51.3	620,486	964	23,508

In Figure 5, the heat transfer coefficient (HTC) multiplied by the surface area A represents the heat transfer capacity of the HX-40. The HTC×A was used to evaluate the capacity of the HX. In Figure 5, the horizontal axis is the pressure drop of the HX-40. The vertical axis is the HTC×A. The horizontal axis and vertical axis are both in logarithmic scales. For different lattices, the results were almost the same. For example, for the HTC×A and pressure drop, the Diamond, SplitP, and Gyroid lattices have almost the same performance results.

In this paper, the gyroid structure was used as an example to illustrate the design and modeling method. Figure 6 shows a single gyroid cell unit with definitions for modeling. A large gyroid structure was assembled with copies of itself by using commercial software such as Solidworks 2016×64 Edition and nTopology 4.23.2. Figure 7 shows the flow chart to design and model the HX. Several iterations were needed to optimize the HX's performance.

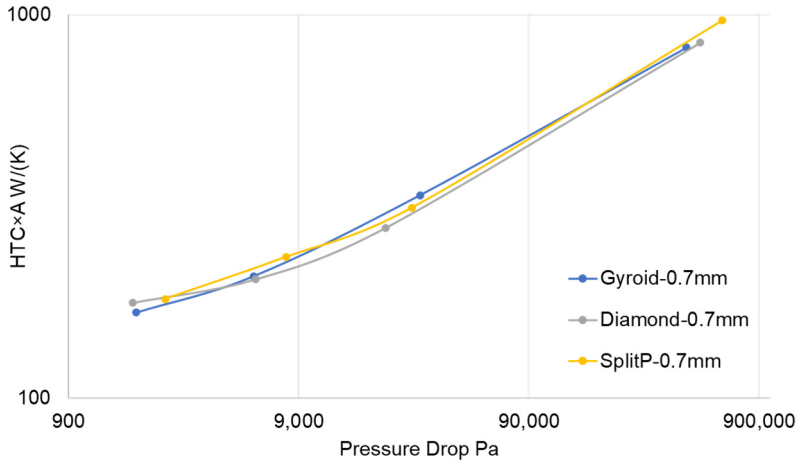

Figure 5. HTC×A of the HX under different input pressure drops.

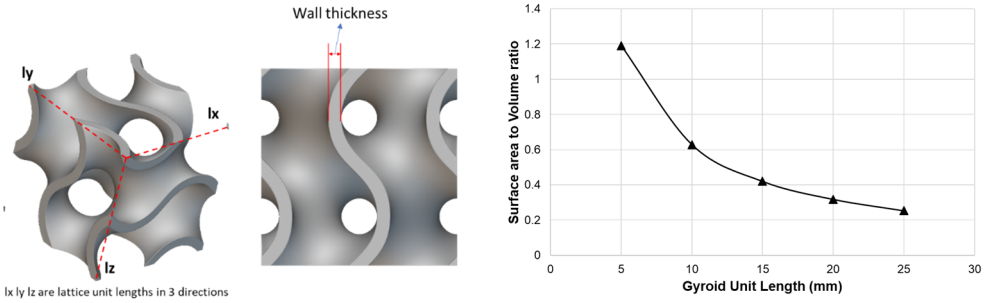

Figure 6. Definition of gyroid lattice parameters. Definition of the gyroid unit length and lattice wall thickness (**Left**) and surface to volume ratio for gyroid lattice with different unit length (**Right**).

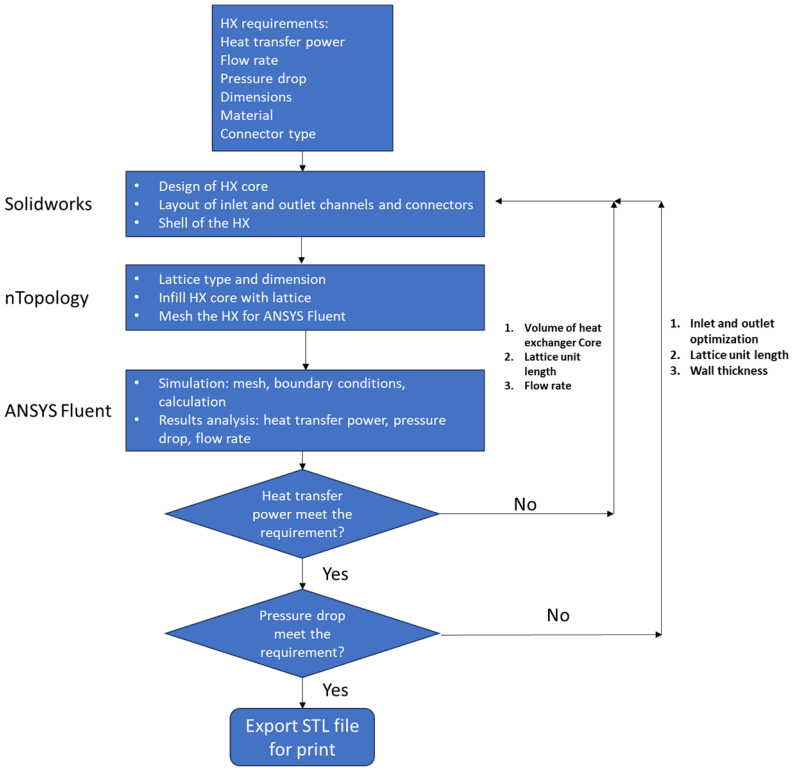

Figure 7. Modeling and design flowchart for TPMS HX.

2.2. Design Examples of TPMS HX

Two high-efficient cubic HXs (named HX70-555 and HX70-101010) were designed for laser AM. The dimensions of HX70-555 and HX70-101010 are shown in Figure 8. The parameters of these two types of cubic HX-70 are shown in Table 3. The material of HX-70 was aluminum. HX70-555 had a gyroid unit that was 5 mm in length in three directions, as shown in Figure 9. HX70-101010 had a gyroid unit with a length of 10 mm in three directions, as shown in Figure 10. Fluid A and fluid B indicates fluids (such as water) at different temperatures. The volume of the HX core was mainly used to simulate thermal transfer parameters including surface area, fluid field, heat transfer coefficient (HTC), pressure drop, and heat transfer capacity. Table 4 gives the simulation results under the assumption that the wall thickness of gyroid lattice is 0.3 mm and has a flow rate of 0.48 kg/s.

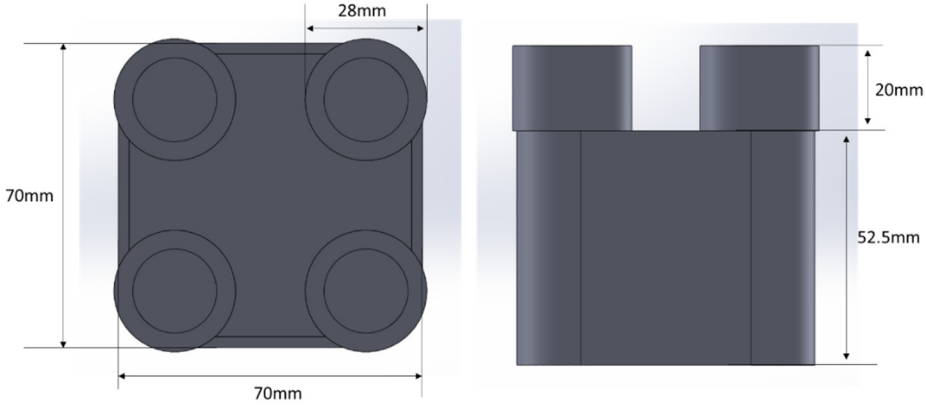

Figure 8. Dimensions of the cubic HX-70.

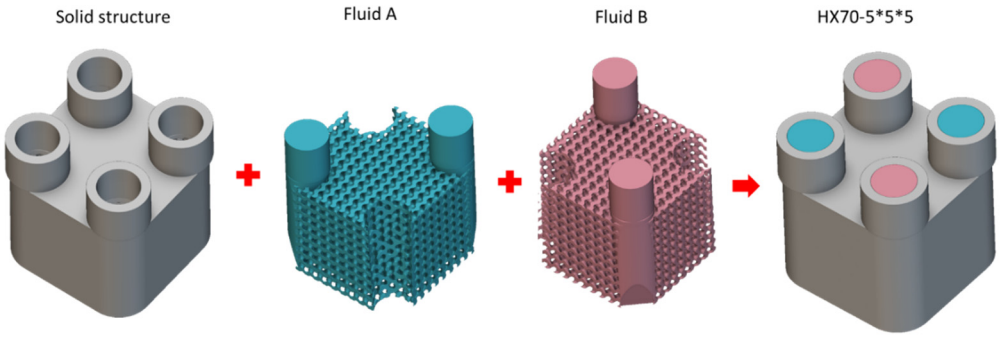

Figure 9. Fluid and heat exchange of HX70-555. Grey color indicates the solid structure. Pink color indicates high temperature water. Light blue indicates the cold water.

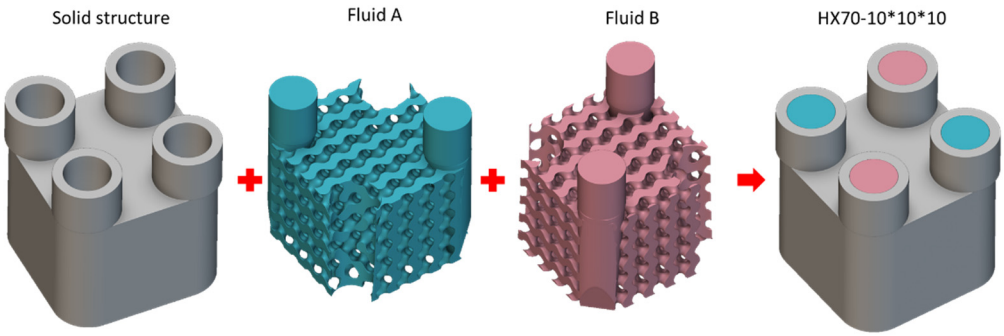

Figure 10. Fluid and heat exchange of HX70-101010. Grey color indicates the solid structure. Pink color indicates high temperature water. Light blue indicates the cold water.

Table 3. Parameters of the two types of cubic HX-70.

Dimension mm	Connector -	Gyroid Unit mm	Wall Thickness mm	Outer Shell Thickness mm	Surface Area m^2	Volume A mm^3	Volume B mm^3	Volume Solid mm^3	Mass Aluminum g
70 × 70 × 72.5	¾ Male NPT	5 × 5 × 5	0.3	2.5	0.1076	70,263	70,201	106,524	288.7
70 × 70 × 72.5	¾ Male NPT	10 × 10 × 10	0.3	2.5	0.0508	76,703	76,712	94,229	255.3

Table 4. Simulation results of the HX-70.

	Gyroid Unit Length mm	Gyroid Wall Thickness mm	Interface Area m^2	Flow Rate kg/s	Pressure Drop Pa	Inlet K	Outlet K	Heat Transfer Power W	Solid Material -	Fluid Material -
A	5 × 5 × 5	0.3	0.1076	0.486	9542	355	344.3261	21,788	Aluminum	Water
B	5 × 5 × 5	0.3	0.1076	0.473	9313	310	320.8787	21,612	Aluminum	Water
A	10 × 10 × 10	0.3	0.0508	0.486	5310	355	349.2863	11,663	Aluminum	Water
B	10 × 10 × 10	0.3	0.0508	0.473	5350	310	315.8485	11,619	Aluminum	Water

The heat transfer coefficient (HTC) was used to compare the HX with different types of TPMSs. The overall heat transfer coefficient in the clean condition, *Uc*, was calculated as follows:

$$Uc = Qt_{avg}/(LMTD \times A) \quad (1)$$

where Qt_{avg} is total average heat transfer rate, calculated as the average of the hot stream heat transfer rate and the cold stream heat transfer rate, and *LMTD* is the logarithmic mean temperature difference, which is defined as follows:

$$LMTD = \frac{\Delta T1 - \Delta T2}{In(\Delta T1/\Delta T2)} \quad (2)$$

where

$\Delta T1 = T_{hot,in} - T_{cold,in}$ and $\Delta T1 = T_{hot,out} - T_{cold,out}$ are parallel flow;
$\Delta T1 = T_{hot,in} - T_{cold,out}$ and $\Delta T2 = T_{hot,out} - T_{cold,in}$ are counter flow;
A is the effective surface area of the HX.

As shown in Figure 11, the HX-70 unit was compared with the commercial 20 kW HX, BT3×8-20. The two main work conditions of BT3×8-20 are shown in Table 4. The HX-70 was three times smaller in volume, and at least five times lighter in weight than the BT3×8-20, as shown in Table 5. Additionally, aluminum (Al) alloy is much cheaper than copper alloys or steels.

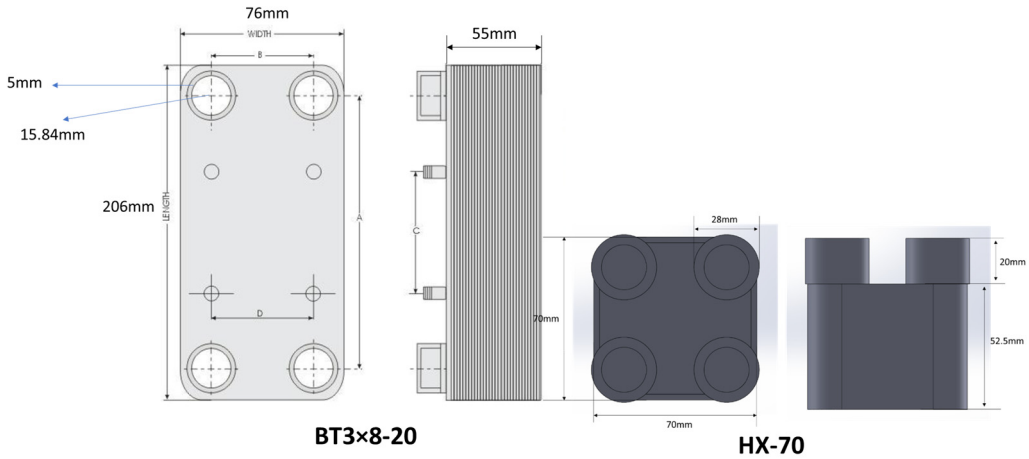

Figure 11. Comparison of the dimensions of BT3×8-20 and HX-70.

Table 5. Two work conditions of the commercial HX BT3×8-20.

	Model	Heat Transfer Power	Boiler Side			Radiant Floor Side		
			Flow	Pressure Drop	Inlet Temperature	Flow	Pressure Drop	Inlet Temperature
		kW	kg/s	Pa	K	kg/s	Pa	K
Condition 1	BT3×8-20	29.31	0.284	13100	366.4	0.139	5516	283.1
Condition 2	BT3×8-20	21.98	0.486	22063	355	0.473	20684	310

The results of the commercial heat exchanger are from the documents downloaded from the official website of the manufacturer. Commercial heat exchanger BT3×8-20, with a heat transfer capacity around 20 kW, met our requirements. At the same time, the BT3×8-20 is a heat exchanger with high efficiency. Based on the parameters shown in Table 6, the performance of the HX-70 can be evaluated by comparing with the commercial heat exchanger.

Table 6. Parameters of commercial units, HX BT3×8-20 and HX-70.

	Dimension	Effective Surface Area	HX Core Volume	Material	Mass
	mm	m^2	mm^3	-	g
BT3×8-20	206 × 76 × 47.75	0.235	519,256	Cooper and Steel	1592
HX-70	70 × 70 × 72.5	0.0508~0.1076	166,000	Aluminum	230~330

2.3. Modeling and Simulation Results

The conjugate heat transfer (CHT) model HX-70 in ANSYS Fluent was analyzed in order to calculate the performances of the heat exchangers infilled with gyroid lattice. The HTC and the pressure drop were calculated by the CHT model HX-70. The flow field and temperature field are shown in Figures 12 and 13.

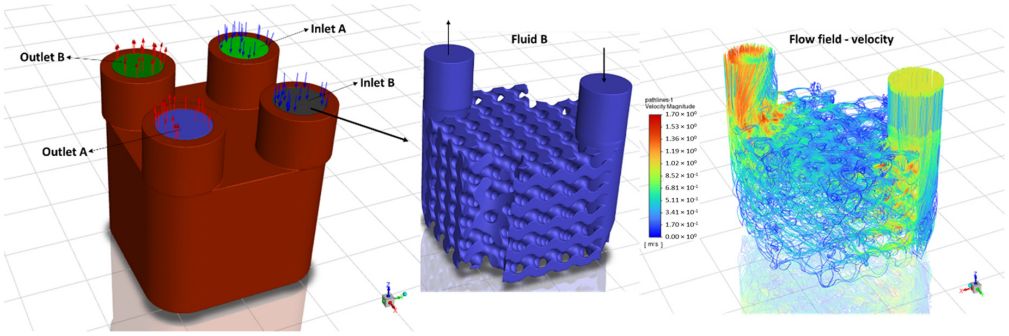

Figure 12. Conjugate heat transfer (CHT) model HX-70.

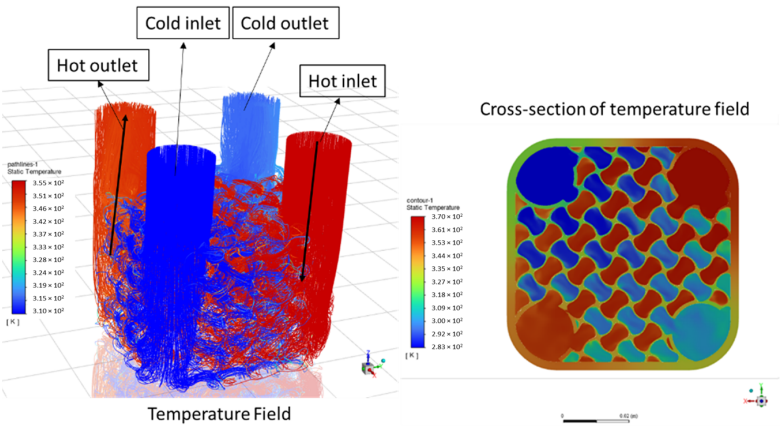

Figure 13. Thermal field calculated by conjugated models of HX-70.

The impact of thickness and thermal conductivity on HTC and pressure drop were investigated by using the flow chart in Figure 7. Figure 14 shows the normalized HTC as a function of thermal conductivity for three different gyroid wall thicknesses: 0.32 mm, 0.64 mm, and 1.31 mm. In the simulation, all the data, with a variety of thicknesses, were normalized to the maximum HTC (W/K.m^2) or thermal capacity (Watt) in the simulated range of thermal conductivity from 0.1 to 1000 W/m·K. Obviously, the highest thermal conductivity and lowest wall thickness gives the maximum HTC or thermal capacity. This shows that the HTC or thermal capacity is less sensitive to the thickness change. A change of less than 5% occurs when the thickness changes from 0.32 mm to 1.31 mm. More interestingly, when the thermal conductivity is higher than 100 W/m·K, less than a 10% change in HTC or thermal capacity occurs when varying thermal conductivity from 100 to 1000 W/m·K. This is very important for cost and weight reduction of HXs, because Al alloys can be used to obtain comparable results with copper alloys.

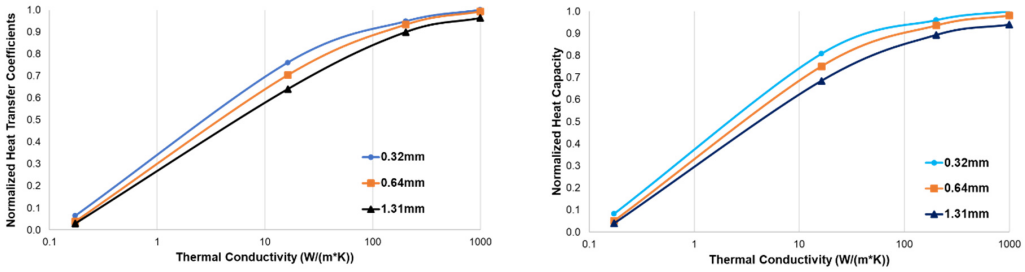

Figure 14. Normalized HTC (**Left**) and thermal capacity (**Right**) as a function of thermal conductivity for three different gyroid wall thicknesses.

The pressure drop in the HX is shown in Table 3. The HX-70 performances were compared with the commercial HX, BT3×8-20, as is shown in Figure 15. It shows that a two times reduction in size, a two-to-three times reduction in pressure drop, and a two-to-three times increase in heat transfer coefficient can be achieved for a 3 × 3 × 3 inch^3 gyroid HX (HX70-555, 0.3 mm wall thickness and 5 mm gyroid unit length) in comparison with a commercial 20 kW plate HX (model BT3×8-20, dimension 3 × 8 × 2.2 inch^3) at the same flow rate. These unprecedented features make the TPMS HX stand out, and deserves further intensive investigation.

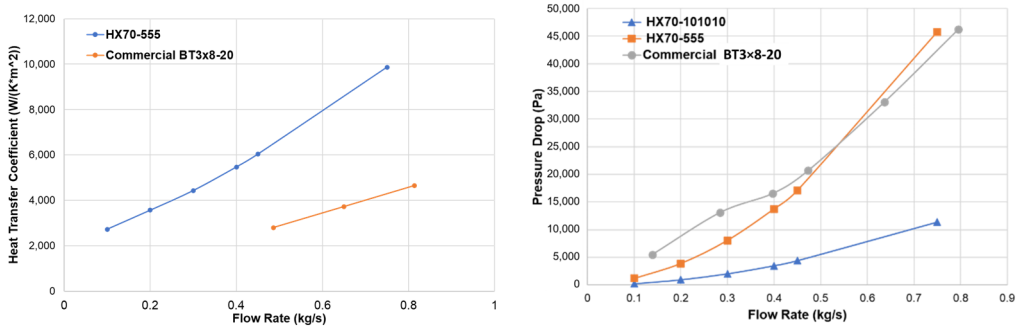

Figure 15. Comparison between gyroid structure HXs and commercial plate type HX (BT3×8-20) at various flow rates. (**Left**) Heat transfer coefficient (HTC), (**Right**) pressure drop.

The temperature field of the HX-70 (capable of 20 kW thermal power management) is shown in Figure 16 (Left), which was calculated by the ANSYS Fluent. The mechanical stress of the HX70-101010−0.3 mm, made from aluminum under 2 MPa water pressure in one volume, was about 30 MPa.

The distribution of the temperatures may result in thermal stress in the HX-70 during operation. The thermal stress of the HX-70 was calculated based on the temperature field. The temperature difference was 40 K for water fluid. The thermal stress of the HX-70 is

shown in Figure 16 (Middle). The maximum stress was about 47.5 MPa, much less than aluminum strength (240 MPa).

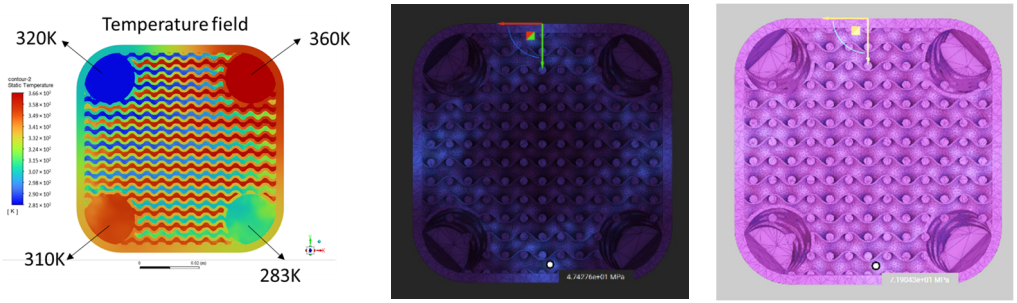

Figure 16. (**Left**) Thermal field simulated by conjugated models. (**Middle**) Thermal stress of the HX. (**Right**) The stress under thermal load and fluid pressure.

The results under both thermal load and fluid operation pressure are shown in Figure 16 (Right). The water fluid pressure load was set at 2 MPa. The maximum stress of the HX-70 was about 72 MPa, which is still less than aluminum (240 MPa), and comparable with the strength of plastic PC.

3. Additive Manufacturing of Gyroid HXs

The inlets and outlets of the HXs described above were designed to make the fluids transfer to the gyroid structure sections. Figure 17 gives the drawings. This section was not optimized to reduce the resistance for flow to optimize pressure drop. However, the HTC and thermal transfer capacity should not be impacted and should allow us to further optimize the TPMS structures.

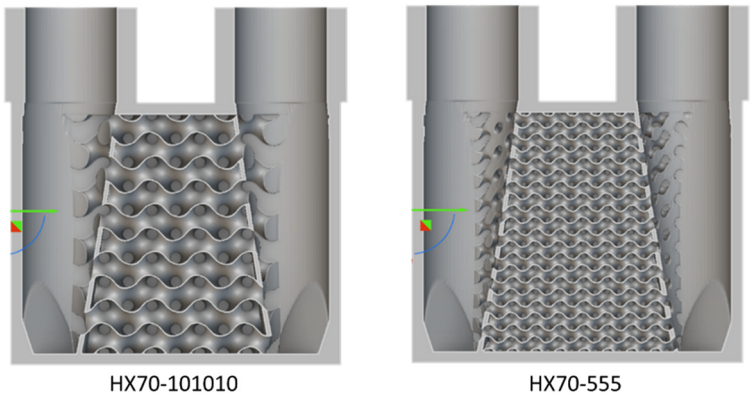

Figure 17. Inner structure of the cubic HX-70, showing the inlet and outlet channels.

Our in-house built AM machine, which printed the HX-70, was able to print metal and ceramic parts using a powder bed fusion method and a direct metal laser melting process. Operators can import STL files, slice and hatch them to create laser marking commands, and print objects. Table 7 lists the optimized AM parameters for the fabrication of HXs.

Table 7. AM parameters for TPMS HXs.

	Layer Height mm	Hatch Mode -	Hatch Line Distance mm	Laser Power W	Laser Scan Speed mm/s	Printing Time h
HX-70	0.45	Line	0.09	140	100	70~80

3.1. Leakage Test and Analysis

Leakage between the two fluid channels (A and B) in the HX cannot be allowed. In order to test the leakage, one of the channels had water added to it. If the other channel leaked water after several hours, it indicates that the two channels are interconnected with each other somewhere. Figure 18 shows the devices fabricated with our in-house AM system and control software. It was also cut in the middle in order to measure the gyroid structures and the quality. We found that the printed aluminum HX had no water leakage to adjacent channels.

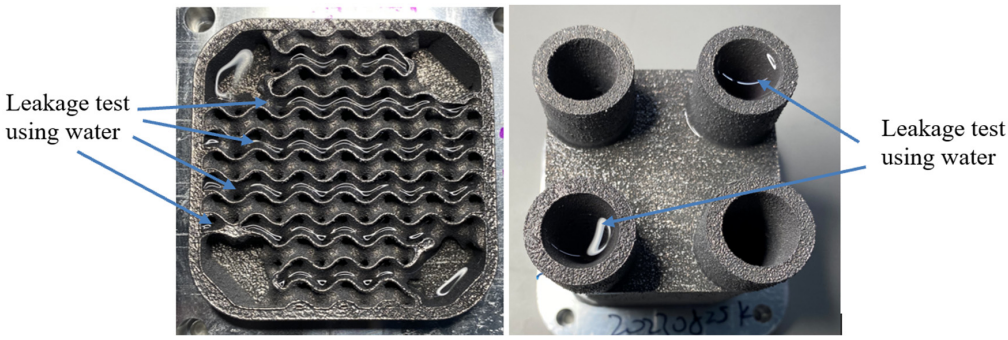

Figure 18. Additively manufactured gyroid HX tested with water: (**Left**) partial HX to test water leakage and wall thickness. (**Right**) a complete HX.

From our intensive investigation, the leakages were mainly located at the interface between the gyroid structure and the bed plate. The main reason as that there was a low-quality domain at the interface. The height of the domain was about 10 µm. If one layer was located within this domain, the layer would be low quality and may result in leakage at this layer. The low-quality domain, labeled red in Figure 19, was generated in the mesh procedure and is hard to be eliminated. The layer height can be changed in order to avoid a low-quality domain. If the layer is not within the low-quality domain, the layer may have good quality and can reduce the risk of leakage. Before printing, the layer quality at the interface needs to be carefully checked. The layer with low quality needs to be avoided by choosing the proper layer height.

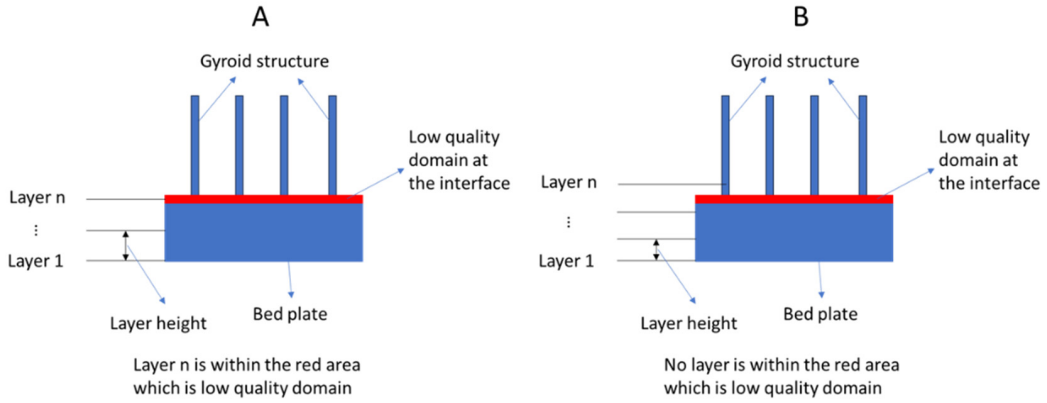

Figure 19. The interface layer distribution at different layer heights. ((**A**) means bad quality slice method and (**B**) means good quality slice method).

3.2. Wall Thickness and Density Test of Gyroid HXs

A partial HX (HX70-555, 0.5 mm wall thickness) was polished in order to test its thin wall quality in terms of thickness, relative density, and uniformity. Density was confirmed with the microscope image method and the Archimedes method. The device was divided into four sections in order to check the gyroid structures, as shown in Figure 20.

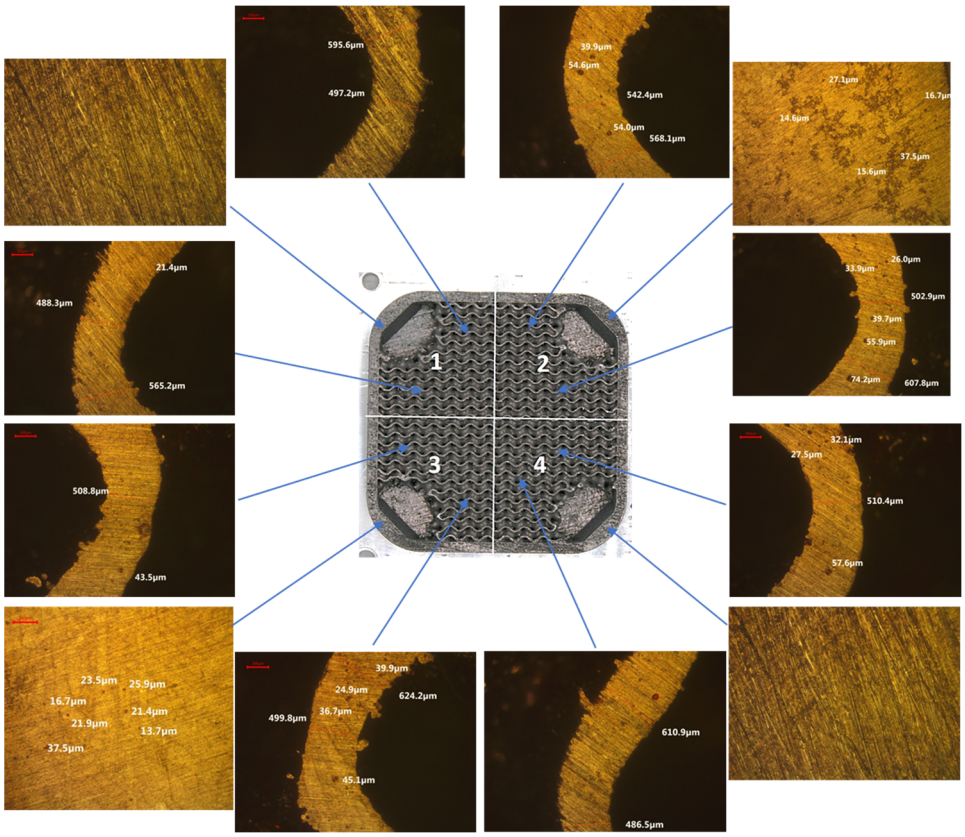

Figure 20. Gyroid wall thickness and relative density measurement results. A result of 98% relative density and 500 μm thickness was achieved, with an excellent uniformity control.

From the measurement, the thicknesses of the gyroid structures were within 450–600 μm. Both the gyroid structures and enclosure walls had a relative density higher than 97%. Figure 21 shows the relative density tested at four randomly selected locations. Very few defects were observed. The sizes of the defects were within 14–50 μm.

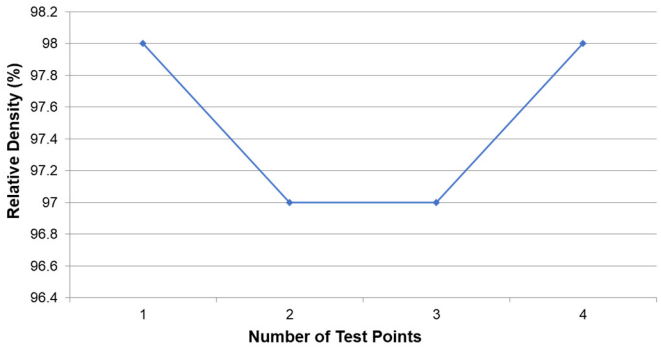

Figure 21. Relative density measurement results at four randomly selected locations.

3.3. Performance Test of Gyroid HXs

After checking and assuring that there were no water leakages for the fabricated HXs, connectors were made for thermal testing. As shown in Figure 22, four ports of the HX were threaded manually with a ¾ NPT male thread. Four adapters were used to covert the male thread to a female thread. Rubber rings were installed on each adaptor in order to prevent water leakage.

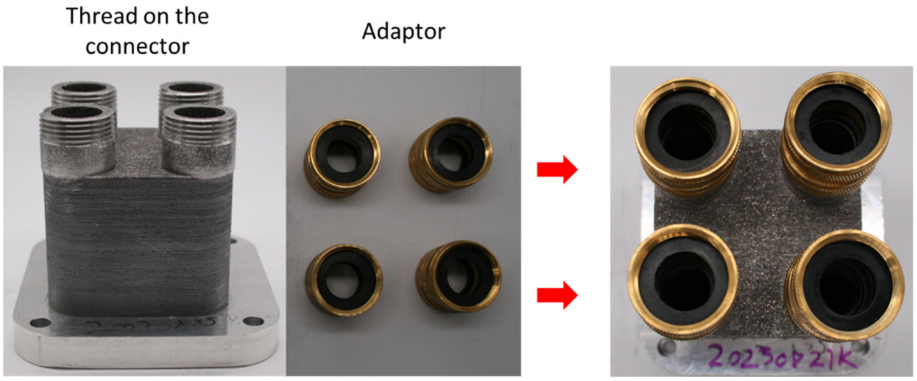

Figure 22. HX assembled with adaptors.

Figure 23 shows the schematic of the experimental setup. The heat exchangers being tested were mounted vertically on a metal plate. Water pressure was measured by pressure transducers that were tapped into the pipe located four-pipe-diameters upstream to the heat exchanger inlet and ten-pipe-diameters downstream to the heat exchanger outlet. Water temperatures were measured using T-type thermocouples mounted through a pipe elbow in the center of the upward pipe. The water volumetric flow rate was measured by using paddlewheel flowmeters located downstream of the heat exchanger, with a straight pipe length of twenty-pipe-diameters upstream to the flowmeter and ten-pipe-diameters downstream to the flowmeter. While hot water was generated using a gas-fired boiler with a nominal input capacity of 58.3 kW, cold water was generated using an air-cooled chiller with a nominal capacity of 10 ton.

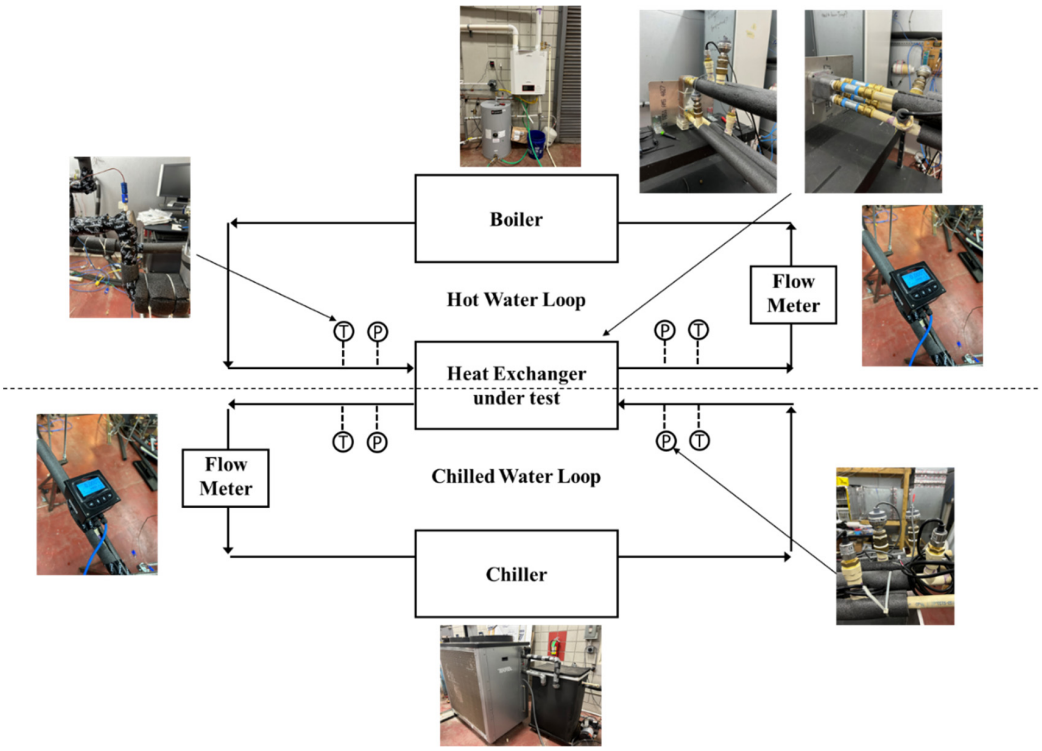

Figure 23. Schematic diagram of the HX testing setup (T means temperature sensor and P means pressure sensor).

Figure 23 shows the target testing conditions. The experimental test was conducted in accordance with ANSI/AHRI Standard 400 (I-P). The experimental data were considered to be valid only if the heat balance was within ±5%. Errors in the tested heat capacity caused by the inaccuracy of the sensor can be within ±1.2%, which is relatively low. It should be

noted that some combined conditions of flow and hot side inlet temperature were found to be unachievable in the testing process due to constraints in heating equipment capacity and pumping power in the testing laboratory. Table 8 were the testing conditions including the temperature and flow rate at the inlet of cold side and hot side.

Table 8. Target testing conditions.

Test ID	Hot Side Inlet Temp K	Cold Side Outlet Temp K	Hot Side Flow kg/s	Cold Side Flow kg/s
1	349.9	291.5	0.1	0.1
2	349.9	291.5	0.2	0.2
3	349.9	291.5	0.3	0.3
4	349.9	291.5	0.4	0.4

The hot side heat transfer rate $\dot{q}_{hot}$ was calculated as

$$\dot{q}_{hot} = \dot{M}_{hot} \times Cp_{hot} \times (T_{hot,in} - T_{hot,out}) \quad (3)$$

where
$\dot{q}_{hot}$ = hot side heat transfer rate, kW;
$\dot{M}_{hot}$ = hot side water volumetric flow rate, kg/s;
Cp_{hot} = hot side water specific heat, J/(kg*K);
$T_{hot,in}$ = hot side water inlet temperature, K;
$T_{hot,out}$ = hot side water outlet temperature, K.

The hot side heat transfer rate $\dot{q}_{cold}$ was calculated as

$$\dot{q}_{cold} = \dot{M}_{cold} \times Cp_{cold} \times (T_{cold,out} - T_{cold,in}) \quad (4)$$

where
$\dot{q}_{cold}$ = cold side heat transfer rate, kW;
$\dot{M}_{cold}$ = cold side water volumetric flow rate, kg/s;
Cp_{cold} = cold side water specific heat, J/(kg*K);
$T_{cold,in}$ = cold side water inlet temperature, K;
$T_{cold,out}$ = cold side water outlet temperature, K.

The water density and specific heat were determined using the average of inlet and outlet water temperatures. The average heat transfer $\dot{q}_{average}$ was calculated as

$$\dot{q}_{average} = \frac{\dot{q}_{hot} + \dot{q}_{cold}}{2} \quad (5)$$

The heat balance (HB) was calculated as

$$HB = \frac{\dot{q}_{hot} - \dot{q}_{cold}}{\dot{q}_{average}} \times 100\% \quad (6)$$

The heat transfer performances were tested and the results are shown in Figure 24. The summary of the testing results is listed in Table 9. They match the modeling results. This shows that the HX70-555 (5 mm lattice) has a significantly high HTC, thanks to its operating in high turbulent mode. However, the inlets and outlets of the HXs were not optimized for a reduction in flow resistance, so the pressure drop was still high. On-going optimization of entrances to the gyroid HX structures should aim to reduce the pressure level to be comparable to the commercial HX.

Table 9. Summary of the testing results.

	Test ID	Surface Area	Hot Side Inlet Temp	Hot Side Outlet Temp	Cold Side Inlet Temp	Cold Side Outlet Temp	Hot Side Flow	Cold Side Flow	Hot Side Heat Transfer	Cold Side Heat Transfer	Average Heat Transfer	Hot Side Pressure Drop	Cold Side Pressure Drop	LMTD	Uc×A	Uc
		m^2	K	K	K	K	kg/s	kg/s	kW	kW	kW	Pa	Pa	K	W/K	W/(K*m^2)
HX70-555	1	0.1014	349.8	319.9	291.5	321.2	0.105	0.104	12.9	12.8	12.9	9446	9308	28.52	451	4448
	2	0.1014	349.7	321.8	291.5	319.1	0.203	0.202	23.3	23.3	23.3	35,784	35,232	30.42	766	7558
	3	0.1014	347.3	321.6	291.5	315.9	0.291	0.300	30.8	30.5	30.7	73,016	77,290	30.73	998	9839
HX70-101010	1	0.0508	349.9	337.1	291.2	304.3	0.103	0.101	5.4	5.5	5.5	1517	1379	45.75	119	2292
	2	0.0508	349.7	339.3	291.5	302.0	0.208	0.202	8.9	8.8	8.9	4551	3723	47.74	185	3565
	3	0.0508	349.8	340.5	291.3	300.5	0.307	0.304	11.7	11.6	11.7	10,480	9584	49.24	237	4550
	4	0.0508	349.6	341.1	291.5	299.4	0.373	0.397	12.9	13.1	13.0	15,720	16,892	49.91	261	5026
BT3×8-20	1	0.235	349.7	314.6	291.5	327.6	0.108	0.101	15.6	15.2	15.4	1310	1103	22.59	680	2893
	2	0.235	346.6	316.3	291.4	321.4	0.207	0.203	25.8	25.3	25.6	3516	3447	25.11	1018	4334
	3	0.235	338.4	315.1	291.4	314.8	0.309	0.306	29.9	29.8	29.8	8963	8825	23.69	1259	5359
	4	0.235	331.5	312.3	291.5	309.4	0.379	0.401	30.2	30.0	30.1	13,721	14,893	21.47	1402	5966

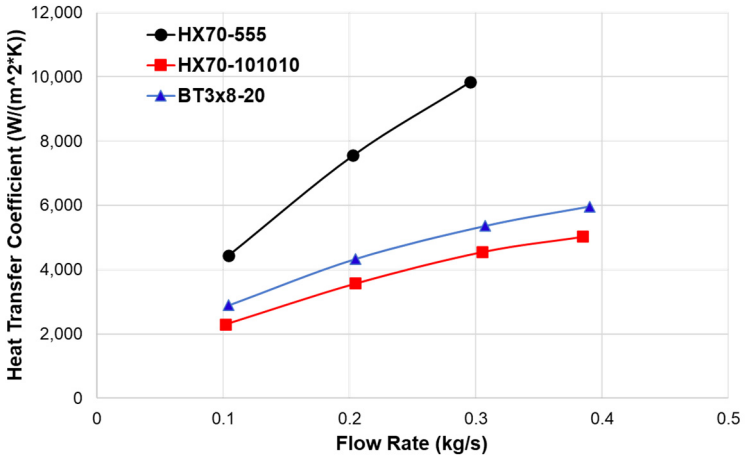

Figure 24. Test setup and experimental results of topology-optimized HXs (5 mm lattice and 10 mm lattice). Comparison of total average heat transfer coefficient of gyroid structure and BT3×8-20.

4. Summary and Conclusions

With advances in AM and features such as high surface-to-volume ratio, high heat transfer coefficients, compact size, and a lighter weight, the TPMS HX is a promising approach for next-generation thermal management. In this paper, the workflow of the design and simulation of the TPMS HX was built. Based on the workflow, the performance of the TPMS HX was evaluated and optimized. The performances of different types of TPMS lattices were compared. Modeling of TPMS HX provides a systematic study on the impact of gyroid wall thickness, lattice unit length, and thermal conductivity. It turns out that, when the thermal conductivity is over 100 W/m·K, the gyroid HX is less sensitive to variations in thickness and thermal conductivity. Finally, 20 kW aluminum heat exchangers were fabricated successfully, and the testing results were comparable with theoretical predictions. The experimental results show that the heat transfer coefficient can be much higher than that in the commercial compact HX.

Author Contributions: Conceptualization, J.L.; Methodology, J.L.; Software, D.C.; Validation, S.B.; Investigation, D.C., K.O. and T.-L.M.; Writing—original draft, J.L.; Writing—review and editing, D.C.; Supervision, S.B.; Project administration, J.L. and S.B. All authors have read and agreed to the published version of the manuscript.

Funding: This research received no external funding.

Institutional Review Board Statement: Not applicable.

Informed Consent Statement: Not applicable.

Data Availability Statement: The data presented in this study are available on request from the corresponding author.

Conflicts of Interest: Authors Jian Liu, David Cheng, Khin Oo, Ty-Liyiah McCrimmon and Shuang Bai were employed by the company PolarOnyx, Inc. The remaining authors declare that the research was conducted in the absence of any commercial or financial relationships that could be construed as a potential conflict of interest.

References

1. Balaji, C.; Srinivasan, B.; Gedupudi, S. Chapter 7—Heat exchangers. In *Heat Transfer Engineering*; Balaji, C., Srinivasan, B., Gedupudi, S., Eds.; Academic Press: Cambridge, MA, USA, 2021; pp. 199–231.
2. Williams, M.; Muley, A.; Bolla, J.; Strumpf, H. *Advanced Heat Exchanger Technology for Aerospace Applications*; SAE International: Warrendale, PA, USA, 2008.
3. Kasim, K.; Muley, A.; Stoia, M.; Ladeinde, F. Advanced heat transfer devices for aerospace applications. In Proceedings of the ASME 2017 International Mechanical Engineering Congress and Exposition, Tampa, FL, USA, 3–9 November 2017; Volume 8.
4. King, W.E.; Anderson, A.T.; Ferencz, R.M.; Hodge, N.E.; Kamath, C.; Khairallah, S.A.; Rubenchik, A.M. Laser powder bed fusion additive manufacturing of metals; physics, computational, and materials challenges. *Appl. Phys. Rev.* **2015**, *2*, 041304. [CrossRef]

5. Careri, F.; Khan, R.H.; Todd, C.; Attallah, M.M. Additive manufacturing of heat exchangers in aerospace applications: A review. *Appl. Therm. Eng.* **2023**, *235*, 121387. [CrossRef]
6. Kaur, I.; Singh, P. Critical evaluation of additively manufactured metal lattices for viability in advanced heat exchangers. *Int. J. Heat Mass Transf.* **2021**, *168*, 120858. [CrossRef]
7. Maconachie, T.; Leary, M.; Lozanovski, B.; Zhang, X.; Qian, M.; Faruque, O.; Brandt, M. SLM lattice structures: Properties, performance, applications and challenges. *Mater. Des.* **2019**, *183*, 108137. [CrossRef]
8. Attarzadeh, R.; Attarzadeh-Niaki, S.-H.; Duwig, C. Multi-objective optimization of TPMS-based heat exchangers for low-temperature waste heat recovery. *Appl. Therm. Eng.* **2022**, *212*, 118448. [CrossRef]
9. Dutkowski, K.; Kruzel, M.; Rokosz, K. Review of the State-of-the-Art Uses of Minimal Surfaces in Heat Transfer. *Energies* **2022**, *15*, 7994. [CrossRef]
10. Reynolds, B.W.; Fee, C.J.; Morison, K.R.; Holland, D.J. Characterisation of Heat Transfer within 3D Printed TPMS Heat Exchangers. *Int. J. Heat Mass Transfer.* **2023**, *212*, 124264. [CrossRef]
11. Ho, J.Y.; Leong, K.C.; Wong, T.N. Additively-manufactured metallic porous lattice heat exchangers for air-side heat transfer enhancement. *Int. J. Heat Mass Transf.* **2020**, *150*, 119262. [CrossRef]
12. Noronha, J.; Qian, M.; Leary, M.; Kyriakou, E.; Brandt, M. Hollow-walled lattice materials by additive manufacturing: Design, manufacture, properties, applications and challenges. *Curr. Opin. Solid State Mater. Sci.* **2021**, *25*, 100940. [CrossRef]
13. Kim, J.; Yoo, D.-J. 3D printed compact heat exchangers with mathematically defined core structures. *J. Comput. Des. Eng.* **2020**, *7*, 527–550. [CrossRef]
14. Dixit, T.; Al-Hajri, E.; Paul, M.C.; Nithiarasu, P.; Kumar, S. Kumar High performance, microarchitected, compact heat exchanger enabled by 3D printing. *Appl. Therm. Eng.* **2022**, *210*, 118339. [CrossRef]
15. Mahmoud, D.; Tandel, S.R.S.; Yakout, M.; Elbestawi, M.; Mattiello, F.; Paradiso, S.; Ching, C.; Zaher, M.; Abdelnabi, M. Enhancement of heat exchanger performance using additive manufacturing of gyroid lattice structures. *Int. J. Adv. Manuf. Technol.* **2023**, *126*, 4021–4036. [CrossRef]
16. van Heerden, A.S.; Judt, D.M.; Jafari, S.; Lawson, C.P.; Nikolaidis, T.; Bosak, D. Aircraft thermal management: Practices, technology, system architectures, future challenges, and opportunities. *Prog. Aerosp. Sci.* **2022**, *128*, 100767. [CrossRef]
17. Chapman, J.W.; Schnulo, S.L.; Nitzsche, M.P. Development of a Thermal Management System for Electrified Aircraft, NASA/TM—2020-220473. Available online: https://ntrs.nasa.gov/api/citations/20200001620/downloads/20200001620.pdf (accessed on 15 March 2020).
18. Waye, S.K.; Lustbader, J.; Musselman, M.; King, C. Air-Cooled Heat Exchanger for High-Temperature Power Electronics. In Proceedings of the 2014 IEEE Compound Semiconductor IC Symposium, San Diego, CA, USA, 19–22 October 2014.
19. Zhang, Z.; Wang, X.; Yan, Y. A review of the state-of-the-art in electronic cooling. *Electron. Energy* **2021**, *1*, 100009. [CrossRef]
20. BCS. *Waste Heat Recovery: Technology and Opportunities in U.S. Industry. U.S. DOE Industrial Technologies Program*; BCS, Inc.: Laurel, MD, USA, 2008. Available online: https://www1.eere.energy.gov/manufacturing/intensiveprocesses/pdfs/waste_heat_recovery.pdf (accessed on 28 March 2008).